PNAS RESEARCH ARTICLE | ENGINEERING

Bistable random momentum transfer in a linear on-chip resonator

Tingyi Gu[a,b,1,2], Lorry Chang[a,1], Jiagui Wu[b,c], Lijun Wu[d], Hwaseob Lee[a], Young-Kai Chen[e], Masudur Rahim[a], Po Dong[e], and Chee Wei Wong[b,c,2]

Affiliations are included on p. 7.

Edited by Yun-Feng Xiao, Peking University, Beijing, China; received February 12, 2025; accepted June 9, 2025 by Editorial Board Member Hui Cao

Optical switches and bifurcation rely on the nonlinear response of materials. Here, we demonstrate linear temporal bifurcation responses in a passive multimode microresonator, with strongly coupled chaotic and whispering gallery modes (WGMs). In microdisks, the chaotic modes exhibit broadband transfer within the deformed cavities, but their transient response is less explored and yields a random output of the analog signal distributed uniformly from "0" to "1." Here, we build chaotic states by perturbing the multimode microring resonators with densely packed silicon nanocrystals on the waveguide surface. In vivo measurements reveal random and "digitized" output that ONLY populates around 0 and 1 intensity levels. The bus waveguide mode couples first to chaotic modes, then either dissipates or tunnels into stable WGMs. This binary pathway generates high-contrast, digitized outputs. The fully passive device enables real-time conversion of periodic clock signals into binary outputs with contrasts exceeding 12.3 dB, data rates of up to 10^7· bits per second, and 20 dB dynamic range.

random number generator | silicon photonics | silicon nanocrystals | TEM | chaotic states

Significance

We consider this work to be crosscutting and fit into the journal's scope for both its scientific significance and impacts on the applications, as this work is 1) an implementation of chaotic modes in the microcavity through nanostructures (high refractive index nanocrystal) rather than macroscopic deformation; 2) explores the time domain response in microresonator supporting chaotic modes, especially with integrated photonic platform rather than the suspended structure of microdisk; 3) reports of *bistable* output in a linear chaotic system; and 4) uses fully passive/powerless on-chip structures for the generation of a random bits sequence on the fly, which typically requires power-consuming electronic components, especially digital–analog conversion.

Hardware random sequence generators support secure communications (1), quantum simulation (2), probabilistic machine learning (3, 4), and regenerative AI (5). The physical entropy sources, such as quantum noise (6, 7), electronic shot noise, and chaotic laser noise (8–14), generate random, continuously varying analog signals. These sources typically require precise threshold tuning to minimize the statistical bias, and advanced analog-to-digital conversions (ADC) to interface with digital communication and computing systems (Fig. 1*A*). Single photon sources can directly generate binary quantum random bins in real time (15–17). Geometric deflection and scattering in resonators disrupt light propagation and circulation, leading to optical loss, mode mixing, and chaotic behavior (18–20). Chaotic modes in deformed microdisks have been associated with broadband waveguide coupling (21), coherent perfect absorption (22), and directional emission (23, 24). These modes can be engineered to achieve specific spectral and temporal responses (25, 26). However, most studies to date have focused on steady-state excitations (23, 27). MRRs, closely related to microdisks, can be lithographically defined and tailored with high precision to achieve any desired geometry. Geometric engineering enables dispersion control, precision mode selections, and multimode operation in MRR (28), but the implementation of chaotic modes has not been reported.

Here, we present an alternative approach using a chip-scale integrated passive microscale component for directly converting an input periodic clock signal into an optical binary pattern *via* a linear chip-scale integrated MRR (Fig. 1*B*). By designing and fabricating a passive multimode silicon nitride (SiN) MRR with high-refractive-index silicon nanocrystal (Si NC)-embedded oxide claddings (Fig. 1 *C*–*G*), we achieved a random bit output exceeding 10^7· bits in a fully passive system. Multimode MRRs were fabricated on a silicon-on-insulator substrate, supporting chaotic modes while retaining the high-*Q* whispering gallery mode (WGM). The waveguide core is made of SiN with a high-refractive index shell of densely packed and randomly distributed Si NCs, inducing mode conversions and chaos within the cavity. We observed a random temporal bifurcation during cavity build-up with pulsed inputs, similar to the recurrent engagement of waves with photonic structures (29). Unlike conventional chaotic optical signal generators, the output of this analog system is directly binary and insensitive to threshold power (Fig. 2*A*). This binary pattern generation occurs in real-time.

Results

Fig. 1*C* is the micrograph of the MRR manufactured through 300 mm wafer run (30, 31) (*Materials and Methods*). A thick (up to 2 μm) hydrogenated amorphous silicon oxide

Author contributions: T.G. designed research; T.G., L.C., J.W., L.W., H.L., M.R., and C.W.W. performed research; T.G., L.W., Y.-K.C., and P.D. contributed new reagents/analytic tools; T.G., L.C., and J.W. analyzed data; and T.G., L.C., and C.W.W. wrote the paper.

The authors declare no competing interest.

This article is a PNAS Direct Submission. Y.-F.X. is a guest editor invited by the Editorial Board.

[1]T.G. and L.C. contributed equally to this work.

[2]To whom correspondence may be addressed. Email: tingyigu@udel.edu or cheewei.wong@ucla.edu.

This article contains supporting information online at https://www.pnas.org/lookup/suppl/doi:10.1073/pnas.2502921122/-/DCSupplemental.

Published July 17, 2025.

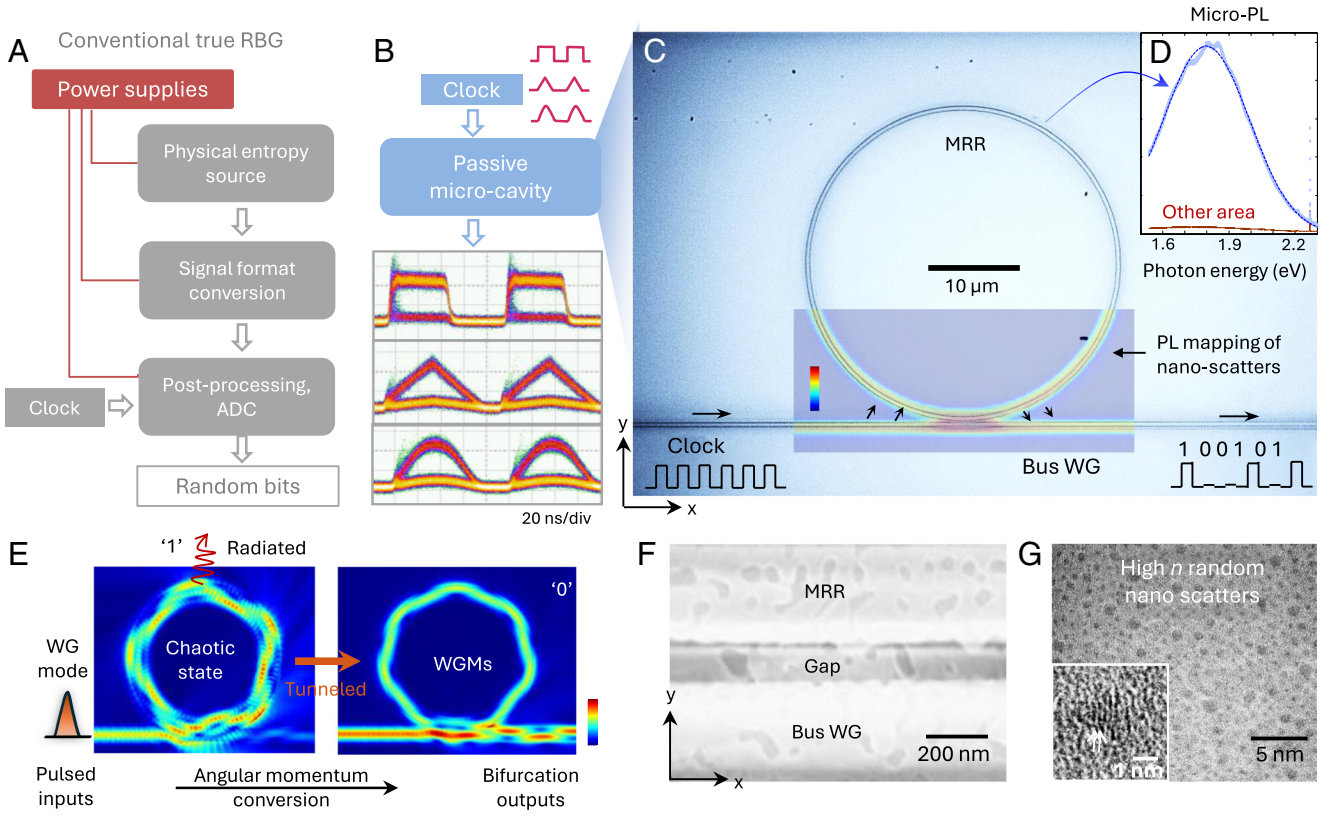

Fig. 1. Silicon nanocrystal perturbed momentum transfer in a passive microring resonator (MRR) toward a chip-scale binary random output. (*A*) System schematic diagram of conventional true random bits generator (RBG). The analog random signal is generated from the physical entropy source, converted or amplified before reaching the postprocessing unit for ADC. (*B*) Physical implementation of fully passive microsystem directly converts input clock signal to clock-wave form defined output binary pattern. *Bottom Inset*: Measured return-to-zero eye diagram of chip-scale random bit pattern directly generated from the device under test. Measurements for rectangular, triangular, and sinusoidal waveform drive at zero detuning, each with the random open-eye pattern generation. (*C*) Optical microscope image of PECVD-grown silicon nitride ring resonator with 40 μm diameters. The densely packed Si nanocrystals are embedded in SiO_2 cladding to the SiN interface. *Middle Inset*: microphotoluminescence intensity spatial map (photon energy of 1.8 eV) superimposed on the device micrograph, with (*D*) typical micro-PL spectra with top excited laser spot (~300 nm) focused on top of the waveguide. (*E*) Short-time snapshots for the full field numerical simulation of the mode, evolving from the waveguide excitation, propagation of chaotic states (*Left*), tunneling to the WGM (*Right*), or dissipation to radiative continuum. (*F*) SEM of the partially etched MRR–waveguide coupling region, exposing nonuniform and deep subwavelength voids hosting silicon nanocrystals in the oxide cladding close to the SiN layer. (*G*) High-resolution transmission electron micrograph (TEM) of silicon nanocrystal (Si NCs) ensemble embedded in the oxide cladding around the silicon nitride waveguide.

($a\text{-}SiO_x$:H) was then deposited on top of the SiN waveguides and MRRs. After high-temperature rapid annealing, Si NCs are found to form on the SiN–oxide interface (32, 33). The measured loaded Q is typically ~75,000 (linewidth of 20 pm) and fiber-chip inverse couplers are included for less than 3-dB coupling loss per facet and total fiber-chip-fiber loss of 14 dB typically (*SI Appendix*, section S1). We used combined microphotoluminescence (micro-PL) mapping approaches to identify the silicon NCs' distribution (*Materials and Methods*). Those silicon NCs were embedded in the oxide matrix surrounding the SiN waveguide, which is identified by the micro-PL mapping (Fig. 1*D*). Tunneling electron microscope (TEM) images identify the average nanocrystal size and density are 3.5 nm and 5×10^{12} cm^{-2}, respectively (*Materials and Methods*). The effective distance between silicon NCs is estimated to be 4.4 nm. The crystalline cores are consistent with diamond cubic silicon. Silicon (220) plane fringes are in the middle with the adjacent spacing ~1.92 Å (Fig. 1*G*). After selectively removing most of the top oxide through wet etching (Fig. 1*F*), the material nonuniformity is verified (which leads to guided modes conversions and chaos). Note the densely packed silicon NCs significantly increase the effective index of the local oxide to be 2.2 (~200 nm thick). The hybrid waveguide has ~40 modes and can support chaotic mode with silicon NCs-assisted mode diffusion (representative cross-sectional mode profiles shown in Fig. 3 *B*, *Insets*) (34) (also in *SI Appendix*, Figs. S2 and S3). The pulsed inputs from the bus waveguide first couple to the high-order chaotic modes (*Left* panel of Fig. 1*E*) and then either dissipated or converted to the WGM (*Right* panel of Fig. 1*E*). If the involved mode is far away from the critical coupling point, minimal attenuation of the transmitted light pulse is expected (represented as "1" state on the transmitted through port). The other mode is close to the critical coupling point, resulting in significant attenuation of the transmitted signal (named "0" state on the transmitted port).

We use simple coupled mode theory (CMT) to describe the dynamic tunneling and coupling between the photon densities in WGM and chaotic modes (21, 31) (*SI Appendix*, section S2):

$$\begin{pmatrix} \dot{a_m} \\ \dot{a_{ch}} \end{pmatrix} = \begin{bmatrix} -\left(\frac{1}{\tau_c}+\frac{1}{\tau_m}\right)+\kappa & -\kappa \\ -\kappa & -\left(\frac{1}{\tau_{ch}}+\frac{1}{\tau_m}\right)+\kappa \end{bmatrix} \begin{pmatrix} a_m \\ a_{ch} \end{pmatrix} + \begin{pmatrix} 0 \\ \frac{a_{in}}{\tau_c} \end{pmatrix}, \quad [1]$$

where a_m and a_{ch} represent the photon numbers in the WGM and chaotic fields, while $1/\tau_m$ and $1/\tau_{ch}$ are their optical decay rates,

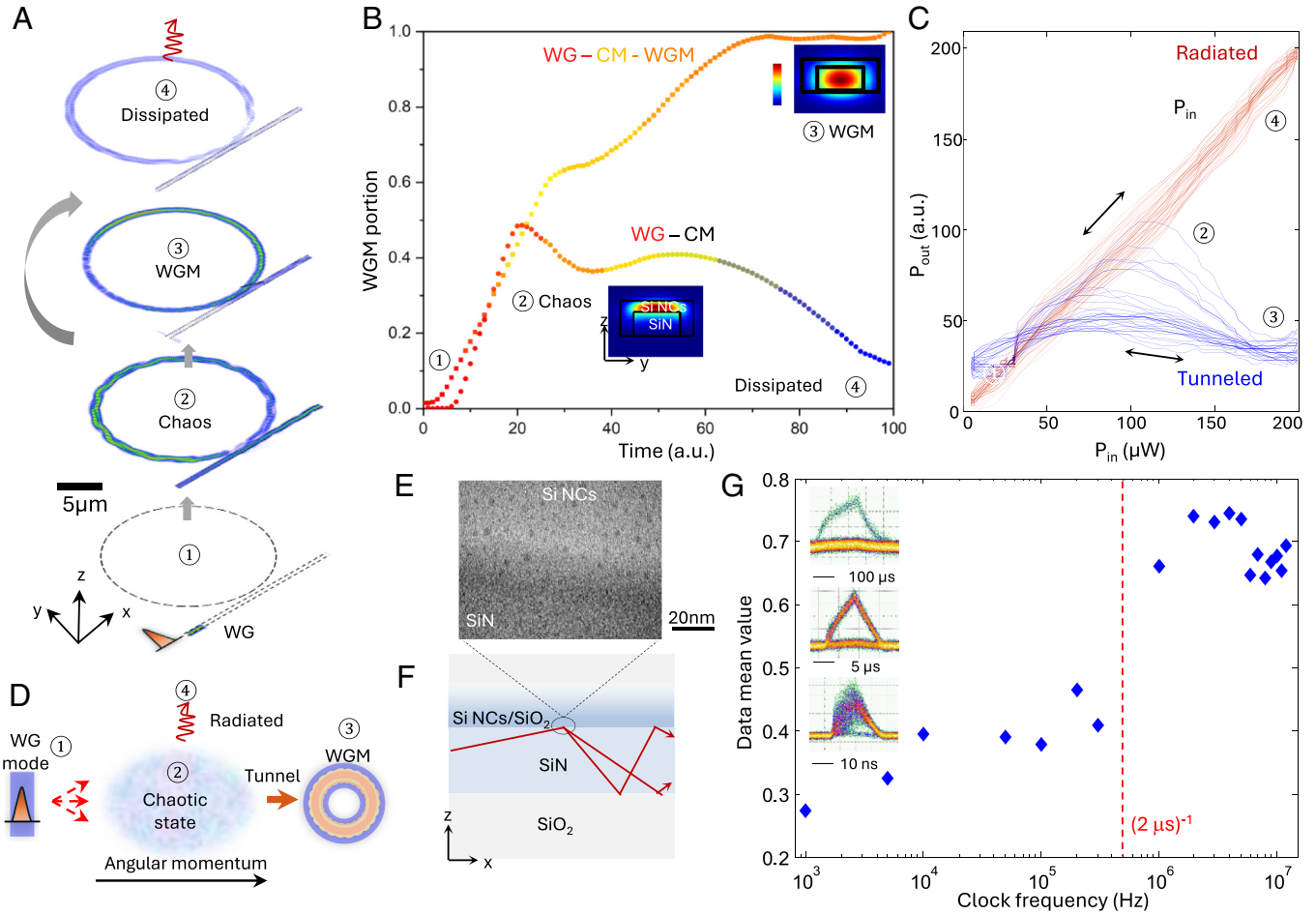

Fig. 2. Bifurcation outputs and verification of random outputs. (*A*) Data mean value versus sampling threshold for the measured data (blue), compared to a typical chaotic source (red). (*B*) Random bit patterns in a two-dimensional plane. Bits 1 and 0 are converted into black and white dots and placed from left to right (from *Top* to *Bottom*); 500 × 500 bits are shown. (*C*) Autocorrelation functions of the output random bits on a linear scale. *Inset*: log scale. Extended data: The resonance fluctuation is majorly induced by room temperature fluctuations and relative refractive index change. The resonance detuning fluctuation leads to on-resonance transmission shifts between 0.8 dB, which is an order of magnitude lower than the random switching we observed, at a much slower rate (~min).

respectively. $a_{in}(t)$ is the complex input field varying rapidly with time (replicating the pulsed inputs). $1/\tau_c$ is the coupling rate between the input waveguide and the resonator. The parameter κ defines the effective tunneling/transfer rate from chaotic modes to WGM. A value of $\kappa = 0$ implies no transfer rate between the states. The existence of silicon NCs, according to the results shown in *SI Appendix*, Fig. S4, potentially modifies κ (*SI Appendix*, Fig. S4). With ultrafast rising edge, the energy conversion from chaotic fields to WGM (*SI Appendix*, Fig. S5*A*). Slower rising edge results in the majority of mode coupling to the chaotic mode (*SI Appendix*, Fig. S5*B*). The WGM has a low extinction ratio (output of 1 state), while the chaotic/high-order modes are close to the critical coupling point, and thus the transmitted photon intensity is significantly reduced (0 state with slower rising edge).

The full field simulation replicates the pathway from chaotic mode to WGM in the NC MRR (Fig. 3 *A* and *B*). Fig. 3*A* shows the representative snapshots of the resonator's spatial electric field intensity distribution from the three-dimensional Finite-Difference Time-Domain (3D FDTD) simulation. First, a pulse signal couples from the bus waveguide into the higher-order modes in the MRR (the radius of the simulated ring is set to be 5 μm as a toy model). Up to 39 picoseconds, the WGM occupancy increases up to 80% and stabilizes as WGM (Fig. 3*B*). If we add random high refractive index structures (replicate the effect of NCs), the WGM portion first decreases, and the chaotic states dissipate as illustrated in Fig. 3*A* (*Top* panel of Fig. 3*A*). Note that the existence of material nonuniformity (Raleigh scatterers of Si NCs) modifies the coupling between the chaotic fields and the WGMs (*SI Appendix*, Fig. S4). Based on the CMT simulations (Eqs. **1** and **2** and *SI Appendix*, section S2), the Si NC–SiN microresonator is likely to operate in the strong coupling regime, in which the coupling rate is higher than the difference between the chaotic mode and WGM dissipation rate, and results in oscillating fields between the two types of modes. The steady state solution of the CMP was used to fit such dynamics (*SI Appendix*, Fig. S6).

To eliminate the possibility of involving optical nonlinearities in the process, we next illustrate the time series of stochastic switching, in the format of output power versus input power, for a triangular input drive with intensity modulation from 8 μW to 200 μW. In the time-domain switching experiment, a triangular waveform with 50 measurements is shown in Fig. 3*B*. The output result reveals two distinct paths: The first path (blue) represents the signal coupling into and staying within the MRR, resulting in low output power (0 state). The second path (red) corresponds to the signal coupling into the MRR but then dissipates, leading to high output power (1 state). Note that while the on-state tracks in the input drive with high fidelity, the time series of the off-state shows temporal fluctuations in some of the off-cycles. We also emphasize the stability of our ring resonance and setup where the background thermal fluctuations are experimentally measured to be typically less than ~0.6 dB (and δ fluctuations of ~0.05), about

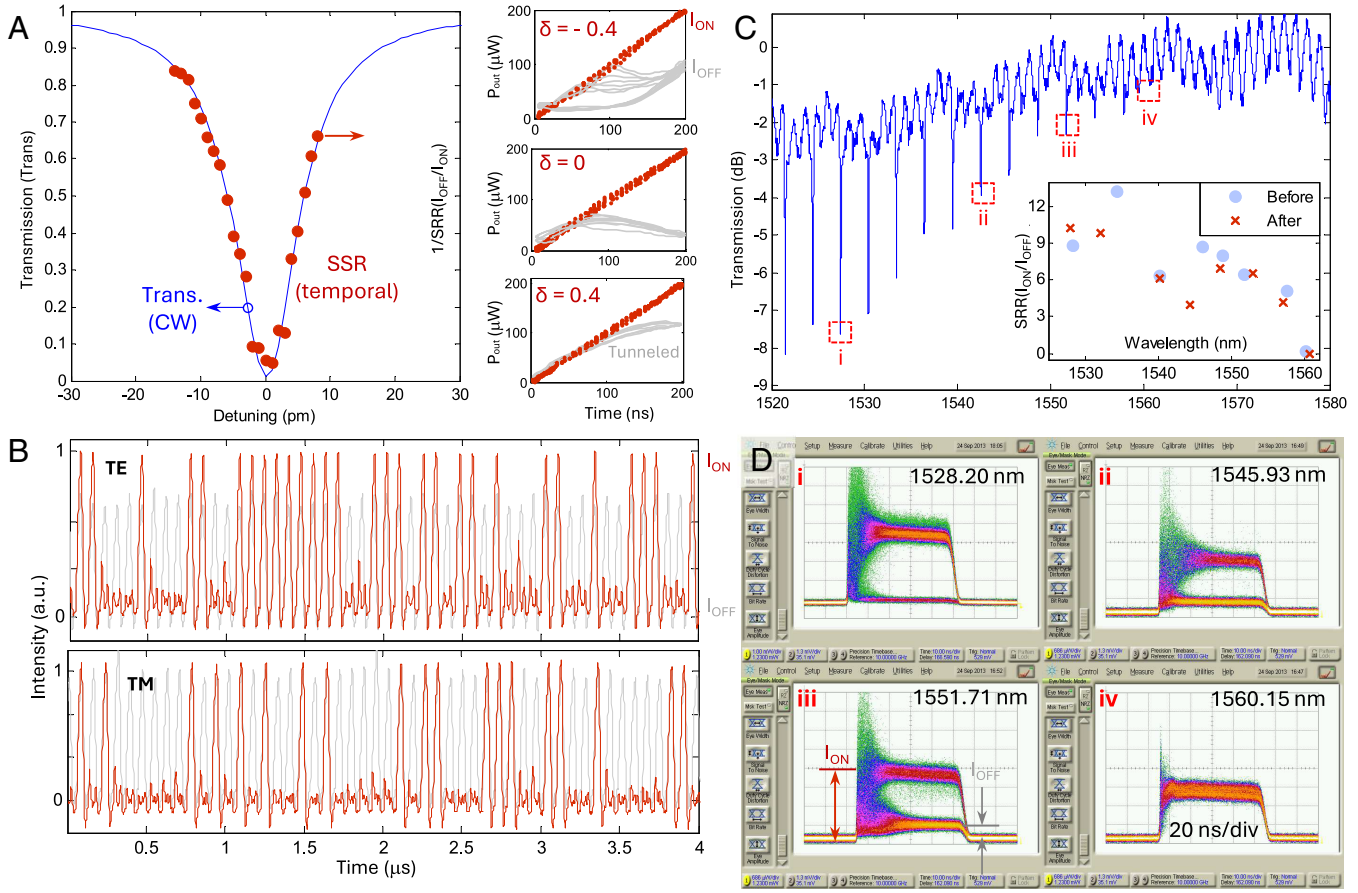

Fig. 3. Transient dynamics of the stochastic binary tunneling. (*A*) Short-time snapshots for the full field numerical simulation of the mode, evolving from the waveguide excitation, coupling to chaotic channel, propagation of chaotic states, tunneling to the WGM, or dissipation to radiative continuum. (*B*) Temporal evolutions of excited WGM portion derived from spatial intensity distribution and two-level modeled value for both tunneled and dissipated paths through chaotic states. *Insets*: Exemplary cross-sectional mode profiles in the Si NC clad SiN WG for chaotic mode and WGM. (*C*) measured time-domain switching for 1 (red) and 0 (blue) states, through a real-time oscilloscope with triangular waveform input. 50-period time series are plotted to illustrate the metastable fluctuations. (*D*) System schematics of nondeterministic tunneling in the microresonator supporting chaotic modes. (*E*) TEM of the interface between silicon oxide and SiN interface. (*F*) Schematic diagram of the mode diffusion and mixing on the SiN–NC interface. (*G*) Measured tunneling or radiation possibilities (data mean value) versus repetition rate (clock frequency) of the input triangular waveform drive, with clock frequencies from 1 to 50 MHz, for P_{in_max} of 100 μW. *Inset*: sampling oscilloscope measured eye diagram. A faster-rising edge results in higher chaotic tunneling possibilities.

an order of magnitude less than the observed on/off switching ratios (further detailed in Fig. 4). We attribute this nondeterministic switching to the mode mixing and diffusion on the SiN – Si NC interface (Fig. 3 *E* and *F*).

This process is repeated on another independent experimental setup (*Materials and Methods*). The second experiment setup involves a triangular waveform generator connected to a tunable laser from a different made, with varying clock frequencies ranging from 1 to 50 MHz. The output is collected by a lensed fiber and connected to a sampling oscilloscope (Fig. 3*G*). The switching nature shows a dependence on the rising edge duration as we observed in Fig. 1*G* (controlled through the clock frequency with the triangular waveform). At the rising edge duration of 0.5 μs, the output shows a sharp transition from ~30% data mean value

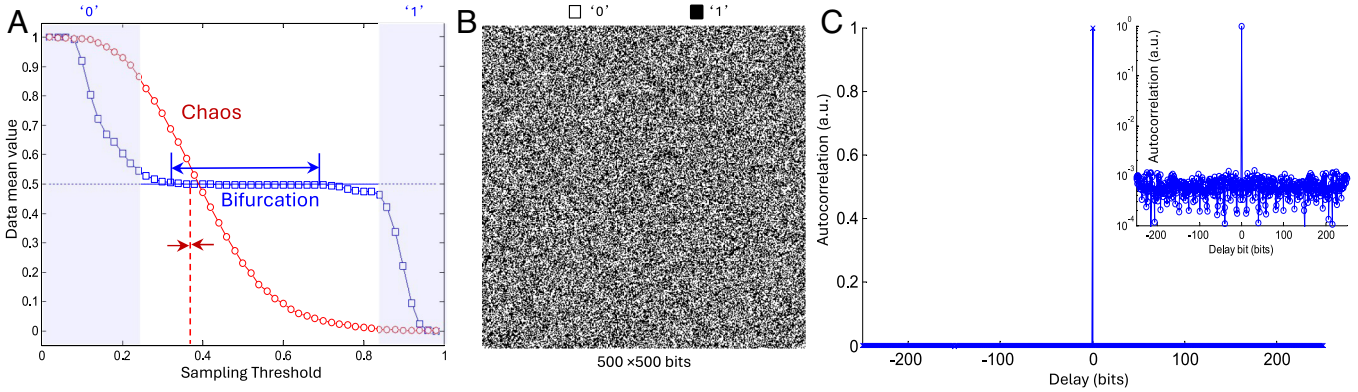

Fig. 4. Measured stability of ring resonance and transmission, for an example 1532 nm resonance, over a 10-min period, for TM (red dots) and TE (green empty squares) respectively. At room temperature, the transmission for the laser on resonance with the ring fluctuates less than 0.8 dB with a 0.3 dB SD, which is almost negligible for ±6 dB observations of stochastic switching between on- and off-states. The normalized detuning δ [defined as $(\lambda_{laser} - \lambda_{cavity})/\Delta\lambda$] fluctuates on an average of 0.03.

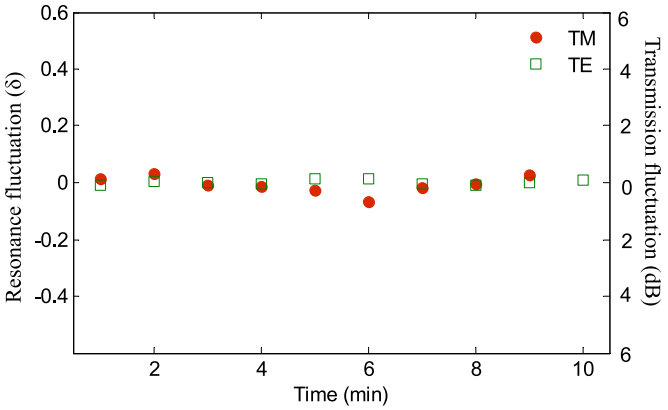

Fig. 5. Binary random pattern generation. (*A*) measured temporal stochastic on/off switching ratios for *both* blue and red-side detuning from the cavity resonance (red dots). A resulting cavity filter lineshape is experimentally superimposed on the broadband stochastic switching. The time domain measurements of the on/off intensity ratio (red dots) match the measured spectral transmission lineshape (solid blue line). *Right* panels are traces of the stochastic switching dynamics, for example, laser-cavity detuning on both sides [$\delta = (\lambda_{laser} - \lambda_{cavity})/\Delta\lambda$]. (*B*) Output time-series transmission of Si-NC clad SiN ring resonator under periodic waveform drive. The *Upper* panel compares the transverse electric (TE; red) versus the transverse magnetic (TM; gray) polarized light on resonance with the Si-NC clad SiN. The *Lower* panel shows the TE polarized input drive at 12 pm (red) and zero (gray) detuning. (*C*) Transmission of 20 μm radius ring resonator. *Inset*: extinction ratio (I_{ON}/I_{OFF}) of the return-to-zero eye diagram of output from 1,528 nm to 1,560 nm, before (empty circles) and after (solid circles) 1150 °C annealing for 1 h in Ar environment. (*D*) Measured eye diagrams for resonances at 1528.20, 1545.93, 1551.71, and 1560.15 nm. Input pulse repetition rate is 10 MHz.

into a higher (~70%) data mean value. The clock frequency can thus be dialed as a method to bias-tune the on/off probability (*SI Appendix*, section S3). The other evidence for the critical role of the rising edge is the waveform-dependent switching possibility even at the same clock rate (Fig. 1*B*). The fast-rising edge of the triangular waveform results in higher possibility of 1 state, while at the same clock rate, triangular and sinusoidal waveforms result in the 0 state.

We overlap the on/off stochastic switching ratio (*SSR*, extinction ratio between the two states measured on the oscilloscope) versus the input laser frequency detuning with the standard optical transmission spectra measurement by sweeping the wavelength of the input tunable laser. The hysteresis loops for two states (gray: 0 or tunneled states, red: 1 or dissipated states) are illustrated in the subpanels. We note that the modulated stochastic switching is observed on *both* positive and negative detuned sides of the Lorentzian cavity. We note the extinction ratio/SSR for 1 and 0 states are maximized near the on-resonance, as the intensity of 0 state follows the transmission outline of the resonance. This is further detailed in *SI Appendix*, Fig. S2, along with the polarization dependence of the *SSR*. When driven with a periodic intensity-modulated waveform such as triangular, rectangular, or sinusoidal waveforms, we observe the stochastic switching in the output transmission over a broadband range of parameters. To support the generality of the stochastic pattern generation, we performed sampling oscilloscope measurements of output waveforms *without* requiring any external electronic digital or pulse pattern generators (as shown in Fig. 1*B* for rectangular, triangular, and sinusoidal waveforms). Here, thousands of successive patterns are mapped, sampled at a 10 MHz input clock frequency. The return-to-zero eye diagram shows open eyes, illustrative of clear bistable switching for tunneling/dissipated states.

The random switching can also be replicated with different polarizations. The time domain series in Fig. 5*B* shows a rectangular drive with 38 ns ramp up/downtime, 13 MHz repetition clock, and laser intensities from 5% to 100% peak power. Note that transverse electric (TE) and transverse magnetic (TM) polarized modes have different resonance wavelengths (*SI Appendix*, Fig. S1). The TE polarization (coupled into the thermally stabilized ring) shows the stochastic bistable on/off switch. At the same wavelength, the transverse magnetic polarization (not coupled to WGM) tracks the input drive precisely. Similarly, TM polarization (at a different input wavelength) exhibits a similar response. At the same wavelength, only the polarization coupled into the resonance exhibits a random switching response (*SI Appendix*, section S4). A slightly different data mean value is observed between the two polarizations, likely due to the different overlap ratios of the many modes with nanocrystal regions. Similarly, after partially removing the nanocrystal, the dissipated state (1 state) possibility significantly reduces, and the transient response replicates the typical MRR response (Fig. 6).

The stochastic switching observed broadband from 1,480 to 1,560 nm. Fig. 5*C* illustrates the cold cavity transmission of the ring (blue line). In this case, the critical coupling occurs around 1,519 nm, as the intrinsic material absorption leads to propagation loss of ~6.8 dB/cm near the absorption peak and reduces to less than 2.3 dB/cm (4.3 dB/cm) at 1,560 nm (1,550 nm) (31). Particularly we illustrate four example resonance modes (i through iv) on the return-to-zero eye diagrams. As shown in Fig. 5*D*, we note the larger fluctuations in the bit switching at 1528.20 nm versus the longer wavelengths, resulting from the fluctuating energy level for 1 state and the noise from the additional amplifier. The extinction ratio of the diagram represents the on-resonance ring characteristics. In the *Inset* of Fig. 5*C*, we further illustrate the extinction ratio for the two states (eye diagrams in Fig. 3*D*) correlates to the steady state measurement for a span of wavelength the telecommunication band laser covers.

The insensitivity of the switching statistics to the sampling threshold is an advantage of such a bistable system, which is implemented in a fully passive MRR structure. We applied a broad range of sampling thresholds for converting the analog waveform into binary digital bits (Fig. 2*A*). The data mean value of output binaries maintains around 0.5 ± 0.002 as the sampling threshold is selected from 35% to 68% to the peak power. The threshold variation range is 33% of peak power, compared to 0.16% tolerance for sampling threshold selection of a standard chaos system (11, 12).

We quantify the statistics of the random bit generation, with the analyzed histograms of the random binary bit sequence shown in *SI Appendix*, Fig. S5. The time-bin of the stochastic switching is then simulated by random binary bit sequences, with probability density versus state duration for both on- and off-states. We obtain similar trends in the modeled P_0 and t_0 versus switch-on probability as in the measurements. We performed autocorrelation measurements of 16 Mbits time series data to examine its random nature further. The randomness can be directly observed by mapping into a bit pattern in a two-dimensional plane of 500 × 500 (Fig. 2*B*). The 30 dB extinction ratio of the noise floor in Fig. 2*C* also confirms the randomness, which can be further extended by increasing the number of datasets (35, 36). The random bit generation here is at 13 MHz, in the higher switch-on state probability (100 kHz clock frequency shows a different state bias, but the random nature is still present).

Discussion

We demonstrate chaotic mode in the multimode high *Q* MRR, enabled by the low loss NCs clad SiN waveguide. The high refractive index contrast silicon NCs are densely embedded in the oxide

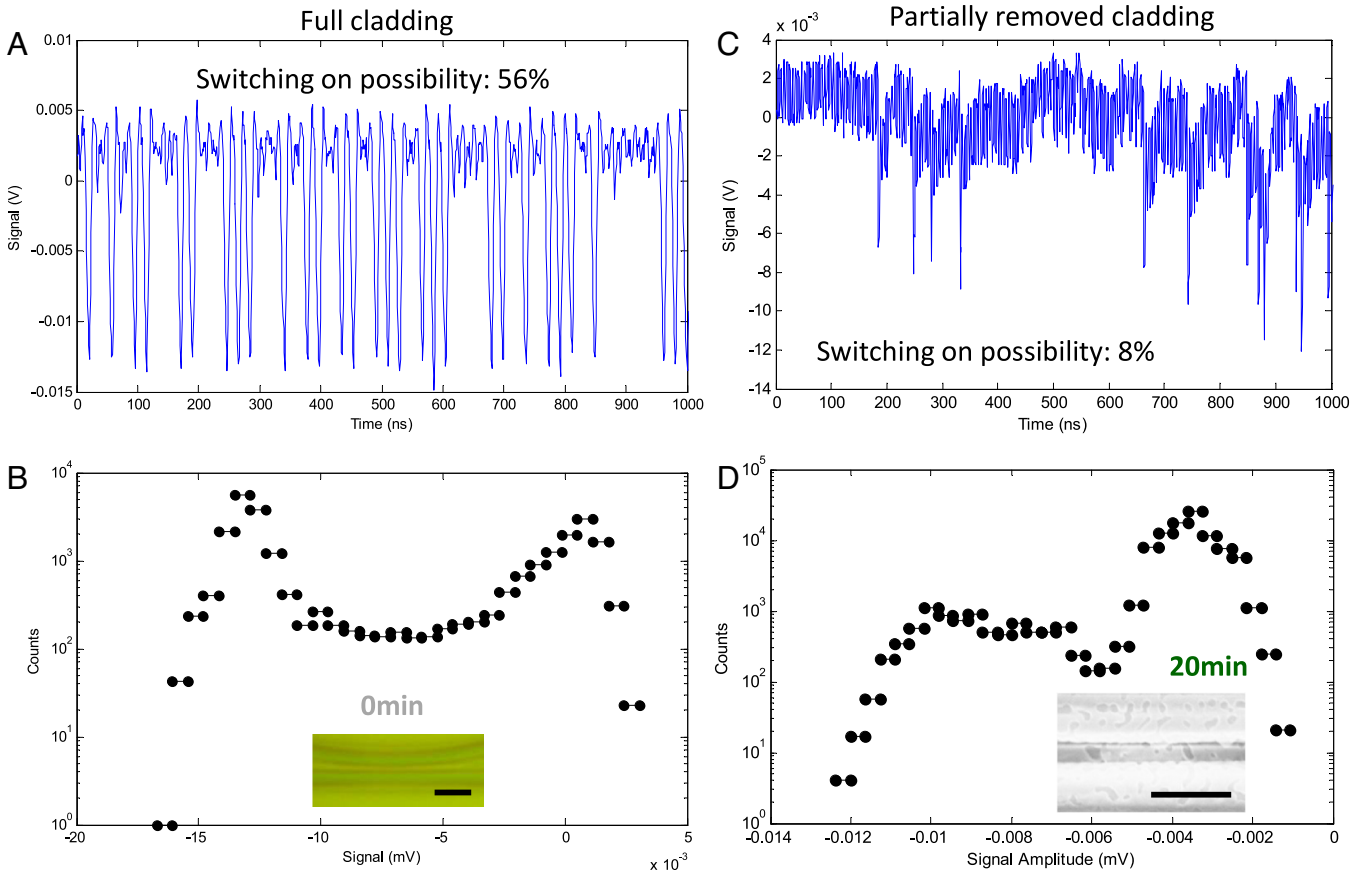

Fig. 6. Reduce the switching possibility of the device with mostly removed silicon NCs. (*A*) The time domain switching dynamics under 13 MHz periodic excitation; (*B*) Histogram of 10^6 bits in (*A*). *Inset*: *Top* optical view of the coupling part between the waveguide and the ring. (Scale bar, 2 μm.) (*C*) Switching dynamics of the device after removing most of the top oxide. A thin-layer oxide (<50 nm) was left to avoid overetching. The input periodic pulse is the same as (*A*). (*D*) Histogram of (*C*). *Inset*: *Top* SEM image. (Scale bar, 2 μm.) The dissipation (nontunneling) possibility reduces from 56 to 8% and 0% for nonetched, partially removed, and totally removed NCs samples, respectively.

gap in the MRR-waveguide coupling region, disturbing the delicate cavity build-up process. The physics enabled bifurcation in the all-optical domain may replace sophisticated electronic processors. The passive devices can directly generate binary outputs with a clear "eye," as captured by a standard sampling oscilloscope used in optical communications. We demonstrated chip-scale random number generation leveraging the random binary angular momentum tunneling through a chaotic state. The stochastic switching behavior is independent of modulated drive laser detuning, wavelength power, and polarization, but only the rising-edge dynamics of the input pulse and the overlap coefficient with the NC region. We studied large dataset distributions and validated them through the internal uncorrelated nature of secure communications and cryptography. Advanced functionalities, such as multichannel wavelength-division-multiplexed random bit generation, can be achieved on a single CMOS-processed ring resonator of ~400 μm^2 footprint. We envision that the compact and fully passive and integrated optical random pattern generator may enable a large-scale photonic reservoir computing system-on-chip, all-optical hardware implementation of diffusion models for regenerative AI (4, 5, 37).

Note that nonlinearity-induced chaos is extensively explored in microring and other chip-scale microresonators, induced by the interplay of different resonators or nonlinear responses (38–40). Those chaotic responses and dynamics are highly sensitive to the input power and only appear on one side of the laser-cold cavity resonance detuning. In our device, symmetric stochastic switching appears symmetrically in both positive and negative tuning, which is delineated from the thermal and laser power fluctuation effects in high Q resonators, where thermal locking (whether for add- or drop-cavity resonances) occurs *only* one side of the detuning when the detuning fluctuates or is swept (41). In our device, the output statistics and temporal evolution are independent of input power. Over 20 dB dynamic range (input power from 5 μW to 500 μW), the switching dynamics are still observed with clear on/off states, elucidating the absence of optical nonlinearity effects on the stochastic nature (Fig. 7).

We also measured the power spectral density of the measured time series. The absence of frequency fluctuations validates that the stochastic nature does not arise from the pump laser, the coupling setup, or the supporting electronics. The sidebands of the amplitude noise are greatly lifted off the output from the device compared to the input clock signal, resembling the random nature of the output, while phase noise shows suppression. The nondeterministic and binary outputs are likely to be the chaotic ring amplified quantum phase noise from the laser source (7).

Materials and Methods

Device Fabrication and Material Characterization. Plasma-enhanced chemical vapor deposition of 6,500 Å SiN_x is processed at a low temperature (350 °C), with low interlayer stress. Deep-ultraviolet nanolithography defines the 1 μm width of the waveguides, followed by reactive etching and resist stripping. Then the silicon oxide is deposited on the waveguide with hydrogen gas, and the silicon nanocrystals are formed in the silicon oxide matrix, seeded by the defects on the interface between PECVD silicon nitride and silicon oxide

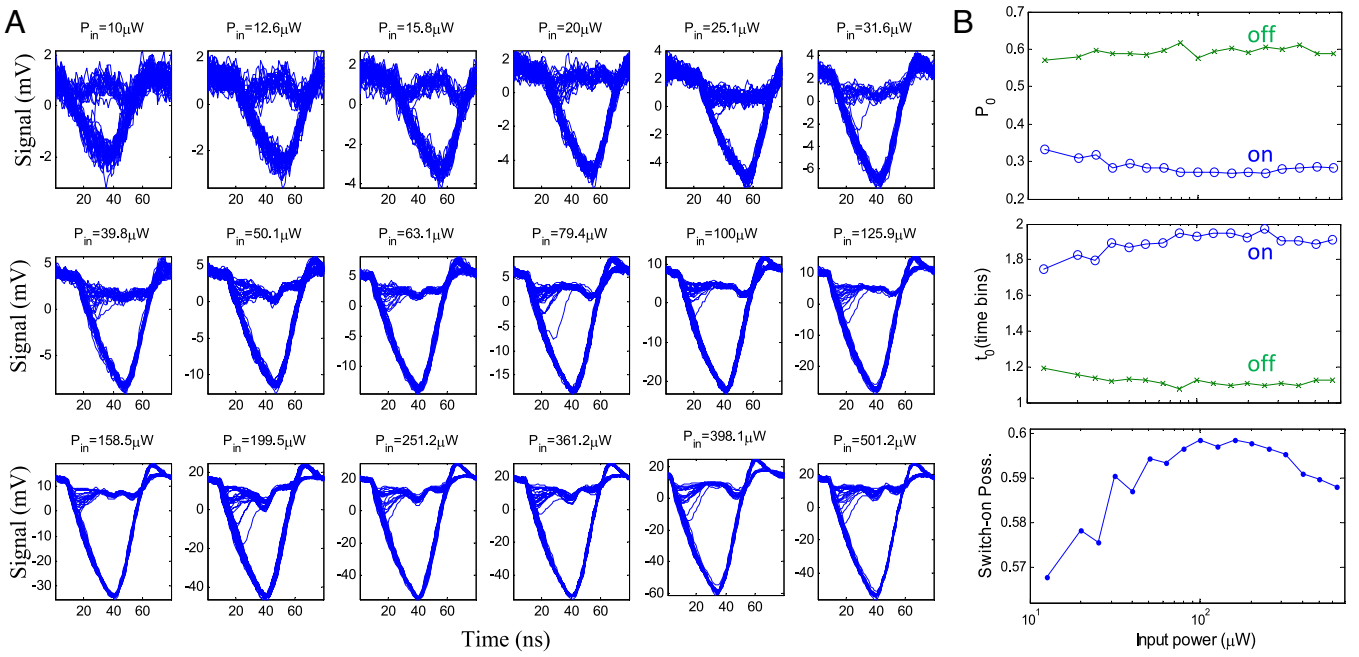

Fig. 7. Power independence of the stochastic switching. (*A*) Superposition of 72 single shots, as the peak of the input power increases from 10 μW to 0.5 mW. (*B*) Parameters of the statistical distribution (amplitude and lifetime) are shown in (*B*), including *P0*, *t0,* and switch on possibility. After synchronizing with input clock, the output distribution follows exponential decay: $P = P_0 e^{-t/t0}$

cladding layer. Photoluminescence spectra of the nanocrystal-ring samples are collected with the RENISHAW micro-Raman system under the 532 and 633 nm laser excitations, with 100 × objective and 1 μm spot sizes (*Inset* of Fig. 1*C*). The TEM sample was prepared by selectively removing the silicon substrate through wet etching. The chiplet was soaked in sodium chloride solution overnight, leaving the top device layer (silicon nitride and silicon nanocrystal) between the oxide layers. The thin film was then transferred to TEM grid for inspection. JEOL ARM200CF (operating at 200 kV, equipped with double aberration correctors and Gatan energy filter system) was used to obtain high-resolution images of the silicon NCs.

Optical Measurements. Stochastic bistable switching is measured and verified on two independent setups. Periodically modulated continuous-wave radiation generated from the tunable laser (Ando AQ4321) is sent onto the chip through a polarization controller and lensed fiber. A built-in power control circuit maintains the optical output intensity stability to within ± 0.01 (0.05) dB or less over 5-min (1-h) durations. An integrated spot size converter reduces the total fiber-chip-fiber loss to 14 dB. Output transmission is collected by a power meter and a high-speed infrared photoreceiver (New Focus 1554B, DC-12 GHz bandwidth). The fast photodetector is connected to the digital phosphor oscilloscope (Tektronix TDS 7404, DC-4 GHz bandwidth). For the return-to-zero eye diagram measurement in the second setup, the tunable laser (Santec TSL), driven by a function generator (HP8116A), sends out different waveforms into the device through a polarization controller (HP11896A). The output signal is amplified by EDFA (Photonetics Fiberam-BT19) with the tunable filter before sending it into a wide-bandwidth sampling oscilloscope (Agilent 86100A with module 86109B).

Optical Simulations. The full field simulations are performed by the 3D FDTD method. The conformal mesh with a spatial resolution less than 1/10 of the local feature size is applied for FDTD simulation. The radius of the microring was set at 5 μm. The center wavelength of the input light source was set at the resonance wavelength, and the duration varies between a few fs to 750 ps for resolving the pulse dynamics-dependent chaotic mode response. The time-varying mode coupling portion is obtained through fitting the FDTD simulation with the CMT model.

Data, Materials, and Software Availability. All study data are included in the article and/or *SI Appendix*.

ACKNOWLEDGMENTS. We acknowledge the fruitful discussions with Seunghwi Kim, Profs. Hui Cao, Xuefeng Jiang, and Giulia Galli. The PL mapping is performed in Dr. Tony Heinz's lab with assistance from Dr. Yilei Li. The high-temperature annealing (for eliminating non-Si-NCs effects such as H-N bonds) postprocessing is performed in Dr. James Hone's lab with assistance from Dr. Xian Zhang (currently at Stevens Institute of Technology). The Tunneling Electron Microscope (TEM) inspection was supported by the U.S. Department of Energy, Office of Basic Energy Science, Division of Materials Science and Engineering, under Contract No. DE-SC0012704. This work is sponsored by the NSF with grant no. 2338546 and Air Force Office of Scientific Research under Contract No. FA9550-25-1-0187.

Author affiliations: [a]Department of Electrical Engineering, University of Delaware, Newark, DE 19711; [b]Mechanical Engineering, Columbia University, New York, NY 10027; [c]Fang Lu Mesoscopic Optics and Quantum Electronics Laboratory, University of California, Los Angeles, CA 90095; [d]Condensed Matter Physics and Materials Science Division, Brookhaven National Laboratory, Upton, NY 11973; and [e]Coherent, Milmont, CA 94538

1. R. G. Gallager, *Principles of Digital Communication* (Cambridge University Press, 2008).
2. S. Asmussen, P. W. Glynn, *Stochatic Simulation: Algorithms and Analysis* (Springer-Verlag, 2007).
3. K. P. Murphy, *Probabilistic Machine Learning: An Introduction* (MIT Press, 2022).
4. Z. Ghahramani, Probabilistic machine learning and artificial intelligence. *Nature* **521**, 452–459 (2015).
5. Y. Song *et al.*, Score-based generative modeling through stochastic differential equations. arXiv [Preprint] (2020). https://doi.org/10.48550/arXiv.2011.13456. (Accessed 1 June 2025).
6. S. Choi *et al.*, Photonic probabilistic machine learning using quantum vacuum noise. *Nat. Commun.* **15**, 7760 (2024).
7. F. Raffaelli *et al.*, Generation of random numbers by measuring phase fluctuations from a laser diode with a silicon-on-insulator chip. *Opt. Express* **26**, 19730–19741 (2018).
8. A. Argyris *et al.*, Chaos-based communications at high bit rates using commercial fibre-optic links. *Nature* **438**, 343 (2005).
9. I. Reidler, Y. Aviad, M. Rosenbluh, I. Kanter, Ultrahigh-speed random number generation based on a chaotic semiconductor laser. *Phys. Rev. Lett.* **103**, 024102 (2009).
10. A. Uchida *et al.*, Fast physical random bit generation with chaotic semiconductor lasers. *Nat. Photonics* **2**, 728 (2008).
11. D. S. Wiersma, Disordered photonics. *Nat. Photonics* **7**, 188 (2013).
12. J. G. Wu *et al.*, Time delay signature concealment of optical feedback induced chaos in an external cavity semiconductor laser. *Opt. Express* **18**, 6661–6666 (2010).
13. C. Abellán *et al.*, Ultra-fast quantum randomness generation by accelerated phase diffusion in a pulsed laser diode. *Opt. Express* **22**, 1645–1654 (2014).
14. K. Kim *et al.*, Massively parallel ultrafast random bit generation with a chip-scale laser. *Science* **371**, 948–952 (2021).
15. T. Jennewein, U. Achleitner, G. Weihs, H. Weinfurter, A. Zeilinger, A fast and compact quantum random number generator. *Rev. Sci. Instrum.* **71**, 1675 (2000).

16. A. Stefanov, N. Gisin, O. Guinnard, L. Guinnard, H. Zbinden, Optical quantum random number generator. *J. Mod. Opt.* **47**, 595 (2000).
17. M. Herrero-Collantes, J. C. Garcia-Escartin, Quantum random number generators. *Rev. Mod. Phys.* **89**, 015004 (2017).
18. H. Cao, Y. Eliezer, Harnessing disorder for photonic device applications. *Appl. Phys. Rev.* **9**, 1 (2022).
19. H. E. Türeci, H. G. Schwefel, P. Jacquod, A. D. Stone, Modes of wave-chaotic dielectric resonators. *Prog. Optics* **47**, 75–137 (2005).
20. S. Yu, C.-W. Qiu, Y. Chong, S. Torquato, N. Park, Engineered disorder in photonics. *Nat. Rev. Mater.* **6**, 226–243 (2021).
21. X. Jiang *et al.*, Chaos-assisted broadband momentum transformation in optical microresonators. *Science* **358**, 344–347 (2017).
22. X. Jiang *et al.*, Coherent control of chaotic optical microcavity with reflectionless scattering modes. *Nat. Phys.* **20**, 109–115 (2024).
23. Z. Liu, Y.-C. Lai, Chaotic scattering in deformed optical microlasing cavities. *Phys. Rev. E* **65**, 046204 (2002).
24. Y.-J. Qian *et al.*, Regulated photon transport in chaotic microcavities by tailoring phase space. *Phys. Rev. Lett.* **127**, 273902 (2021).
25. C.-H. Yi, J. Kullig, J. Wiersig, Pair of exceptional points in a microdisk cavity under an extremely weak deformation. *Phys. Rev. Lett.* **120**, 093902 (2018).
26. S. Bittner *et al.*, Suppressing spatiotemporal lasing instabilities with wave-chaotic microcavities. *Science* **361**, 1225–1231 (2018).
27. S. Wang *et al.*, Direct observation of chaotic resonances in optical microcavities. *Light Sci. Appl.* **10**, 135 (2021).
28. Y. Zhang, K. Zhong, X. Zhou, H. K. Tsang, Broadband high-Q multimode silicon concentric racetrack resonators for widely tunable raman lasers. *Nat. Commun.* **13**, 3534 (2022).
29. F. Xia *et al.*, Nonlinear optical encoding enabled by recurrent linear scattering. *Nat. Photonics* **18**, 1067–1075 (2024).
30. S. C. Mao *et al.*, Low propagation loss SiN optical waveguide prepared by optimal low-hydrogen module. *Opt. Express* **16**, 20809–20816 (2008).
31. T. Gu, M. Yu, D.-L. Kwong, C. W. Wong, Molecular-absorption-induced thermal bistability in PECVD silicon nitride microring resonators. *Opt. Express* **22**, 18412–18420 (2014).
32. J. N. Milgram, J. Wojcik, P. Mascher, A. P. Knights, Optically pumped Si nanocrystal emitter integrated with low loss silicon nitride waveguides. *Opt. Express* **15**, 14679–14688 (2007).
33. R. Tsubata *et al.*, Silicon nanocrystals embedded in nanolayered silicon oxide for crystalline silicon solar cells. *ACS Appl. Nano Mater.* **5**, 1820–1827 (2022).
34. H. Cao, A. P. Mosk, S. Rotter, Shaping the propagation of light in complex media. *Nat. Phys.* **18**, 994–1007 (2022).
35. I. Kanter, Y. Aviad, I. Reidle, E. Cohen, M. Rosenbluh, An optical ultrafast random bit generator. *Nat. Photon.* **4**, 58 (2010).
36. J.-G. Wu, G.-Q. Xia, Z.-M. Wu, Suppression of time delay signatures of chaotic output in a semiconductor laser with double optical feedback. *Opt. Express* **17**, 20124–20133 (2009).
37. R. Laje, D. V. Buonomano, Robust timing and motor patterns by taming chaos in recurrent neural networks. *Nat. Neurosci.* **16**, 925–933 (2013).
38. Z. Ge *et al.*, Broadband random optoelectronic oscillator. *Nat. Commun.* **11**, 1–8 (2020).
39. D. Moreno *et al.*, Synchronization of two chaotic microresonator frequency combs. *Opt. Express* **32**, 2460–2472 (2024).
40. M. Mancinelli, M. Borghi, F. Ramiro-Manzano, J. M. Fedeli, L. Pavesi, Chaotic dynamics in coupled resonator sequences. *Opt. Express* **22**, 14505–14516 (2014).
41. T. Carmon, L. Yang, K. J. Vahala, Dynamical thermal behavior and thermal self-stability of microcavities. *Opt. Express* **12**, 4742 (2004).

Supplementary Information for

Bistable random momentum transfer in a linear on-chip resonator

Tingyi Gu[1,2†*], Lorry Chang[1†], Jiagui Wu[2,3], Lijun Wu[4], Hwaseob Lee[1], Young-Kai Chen[5], Masudur Rahim[1], Po Dong[5], and Chee Wei Wong[2,3]*

[1] Department of Electrical Engineering, University of Delaware, Newark, DE 19711, United States

[2] Columbia University, New York, NY 10027, United States

[3] Fang Lu Mesoscopic Optics and Quantum Electronics Laboratory, University of California, Los Angeles, CA 90095, United States

[4] Condensed Matter Physics and Materials Science Department, Brookhaven National Laboratory, Upton, New York 11973, United States

[5] II-VI Incorporated, 48800 Milmont Drive, Milmont, California 94538, United State

[†]Authors contributed equally, * correspondent authors

S1. Optical and nanostructure characterization of the device

SiNx films are grown by plasma-enhanced chemical vapor deposition (PECVD). The SiH_4 and N_2 gas flow rates are 80 sccm and 4000 sccm, respectively. 400W RF power was applied to reach the SiN deposition rate of 22.8A/s. The growth temperature is kept at 350º. The refractive index of SiN film is measured to be 2.03 [SR1]. After the UV lithography and etching for the formation of waveguide structures, a PECVD SiO_2 layer was deposited on top with gas flows of SiH_4 and O_2.

Since no annealing was performed during the thin film growth, we believe those silicon nanocrystals (NCs) embedded in the oxide matrix were formed through gas-phase synthesis with plasma enhancement, with Hydrogen diffused from PECVD SiN waveguide at the growth temperature of 350º. Since hydrogen is critical for the formation of Si NCs in the oxide matrix, the area away from SiN surface does involve sufficient H in the oxide growth process and thus Si NCs were absent (more details in Fig. S2).

The linear loss of the waveguides is measured by the sampling of different channel waveguide length samples, from 25 mm to 44 mm with a 5 mm step. The fitted transmitted power versus waveguide length with the linear model gives a maximum propagation loss of ~ 6.8 dB/cm at 1520

nm, which is reduced to 4.3 dB/cm at 1550 nm, and further reduced to less than 2.3 dB/cm at 1560 nm. The fiber-to-fiber coupling loss from the two facets is ~ -13.5 dB.

We measured three micro-rings with diameters of ~20, 40 and 70 μm, with loaded, intrinsic quality factor (Q) and FSR respectively of 24,500, 49,000, 8.7nm; 69,600, 175,000, 4.4nm; and 77,300, 244,000, 2.9nm. The intrinsic Q is inversely related to the total loss rate of the resonator, including material absorption loss and scattering loss. The absorption from the chemical bonds (second harmonic absorption of H-N bond near 1520nm) is wavelength dependent while the scattering of the silicon nanocrystals is broadband. Smaller rings exhibit lower Q due to additional bending loss. With the assistance of coupled mode theory analysis, we extract the broadband scattering loss of 1dB/cm, and the maximum linear loss originating from the H-N bond absorption (near 1520 nm) adds another -2.8dB/cm [SR2].

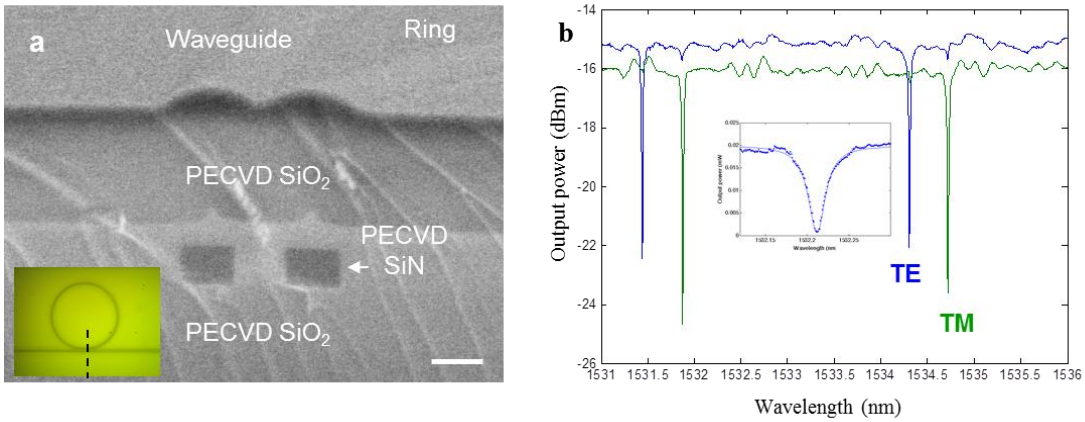

Figure S1 | Structure and linear optical properties of the device. a, SEM of the cross-section of the ring resonator. 650nm PECVD silicon nitride is sandwiched between the PECVD silicon oxide up cladding layer and the thermal oxide lower cladding layer. Scale bar: 1um. Inset: Optical image of top view of the ring, where the dashed line shows the cleaved position for the SEM image. **b,** Output spectrum of TE and TM polarized input with 0dBm input power. Inset: Transmission spectrum of measured modes with a 16 pm linewidth and 14 dB extinction ratio.

All of microresonators across the wafer show random switching behavior, with an extinction ratio and average switching possibility varying with wavelength and radius. The cross-section of the ring-waveguide coupling is shown in Fig. S1a, where the PECVD silicon oxide surrounds PECVD silicon nitride. The high aspect ratio of the silicon nitride waveguide (1μm wide, 0.65μm tall)

distinguished TE and TM modes (as in Fig. S1b). The quality factor can be read by using coupled mode theory to fit the transmission spectrum of one of those modes. The largest ring with 70 μm diameter with a ring-waveguide gap of 0.5μm gives FWHM of ~16pm.

Note that the photoluminescence signal can be attributed to either the defects in SiN or silicon nanocrystals [SR33-SR7]. To track the origin of PL (from the core SiN waveguide or cladding layer), we performed the multi-step wet etching and inspection cycles. The PL intensity reduces with the removal of the top oxide layer (hosting the Si nanocrystals) (Fig. S2).

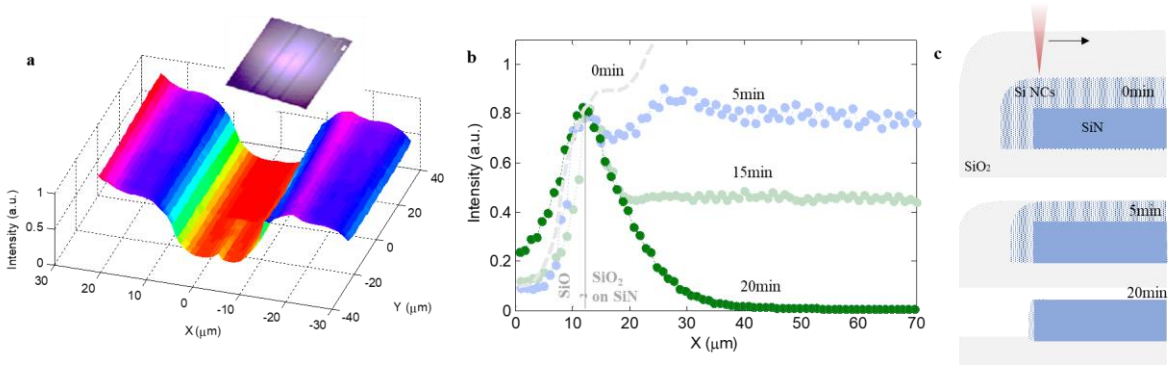

Figure S2 | Confirmation of silicon nanocrystals distribution in cladding layer by wet etching. (a) The photoluminescence intensity mapping on the tip of the waveguide (Inset: optical image). The part with silicon nitride (two sides and middle waveguide) shows a much stronger PL signal than the part without SiN. (b) Map of PL intensity along X axis after 50% BOE wet etching of 0 min (grey dashed line), 5 min (blue dotted line), 15 min (light green dotted line), and 20 min (dark green dotted line). The edge of the SiN is marked in the figure at X=12μm. (c) Schematic device cross-section with different oxide wet-etching time (corresponds to b). The scanning micro-photoluminescent mapping (results in a and b) was obtained through the top incident/collected focused beam.

The additional cladding layer of Si NCs significantly alters the number of supported modes and their effective index in the waveguides (Fig. S3).

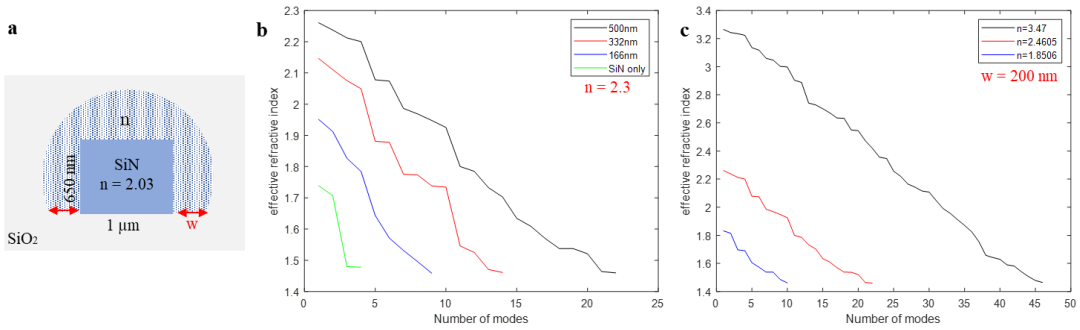

Figure S3 | Waveguide cross-section and effective index of the supported modes. (a) Cross section of the SiN waveguides. The refractive index of the PECVD-grown SiN is measured to be 2.03 [SR1]. (b) Effective index versus supported modes for increasing thickness of the Si NCs embedded oxide layer. (c) With a fixed Si NC embedded oxide layer, increasing the effective index (scales with Si NCs density) results in a higher effective index in many more modes.

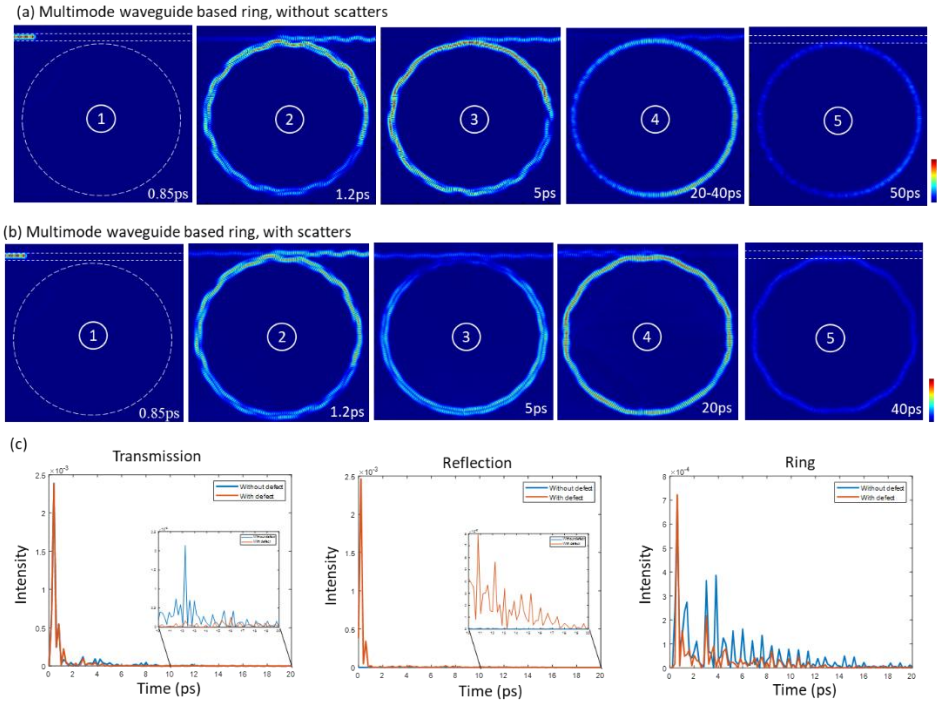

Fig. S4 | Impacts of scatters/defects on the chaotic – WGM mode transitions. (a) Mode dynamics in the multi-mode microresonator without and (b) with deep subwavelength scatters/defects. (c) The intensity dynamics for the monitors placed on the input port, transmitted port and within the resonator, comparing the results without (red) and with scatters (blue). Ring radius: 5 µm.

Then we conducted the 3D FDTD numerical simulations in the multi-mode micro-ring with and without scatters. The first set focuses on the impact of the scatters. A 750 ps pulse excitation was injected into the structure through the bus waveguide (labeled 1 in Fig. R2). As time progresses, chaotic states emerge within the micro-ring, apparent from the unevenly distributed modes around the ring (labeled 2). After a few picoseconds, the occupancy of WGMs increases, and the modes stabilize towards WGMs (labeled 3-4). Finally, the mode dissipated through the radiation/intrinsic loss (labeled 5). Significant difference is observed in stage 3 and 4, after adding the scatters. The forward and backward scattering changes the direction of input light and modifies the mode conversion dynamics in the resonator.

S2. Dynamic tunneling through chaotic states

Parallel to the 3D FDTD simulation, we build analytical modes of coupled mode theory (CMT) to describe the dynamic tunneling and coupling between the photon densities in whispering gallery mode (WGM) and chaotic modes [SR8, SR9]:

$$\frac{da_m}{dt} = -\left(i(\omega_L - \omega_0) + \frac{1}{\tau_c} + \frac{\mathbf{1}}{\boldsymbol{\tau_m}}\right) a_m - \kappa(a_{ch} - a_m) \tag{S1}$$

$$\frac{da_{ch}}{dt} = -\left(i(\omega_L - \omega_0) + \frac{1}{\tau_c} + \frac{\mathbf{1}}{\boldsymbol{\tau_{ch}}}\right) a_{ch} - \kappa(a_m - a_{ch}) + \frac{a_{in}(t)}{\tau_c} \tag{S2}$$

Where a_m and a_{ch} represent the photon numbers in the WGM and chaotic fields, while $1/\tau_m$ and $1/\tau_{ch}$ are their corresponding optical decay rates. ω_L is the angular frequency of the input laser, and the ω_0 is the one for the cold cavity resonance. $a_{in}(t)$ is the complex input field varying rapidly with time (replicating the pulsed inputs). $1/\tau_c$ is the coupling rate between the input waveguide and the resonator. The parameter κ defines the effective tunneling/transfer rate from chaotic modes to WGM. A value of $\kappa = 0$ implies no transfer rate between the states. The existence of silicon NCs, according to the results shown in Fig. S4, potentially modifies κ.

Here we plot the mode dynamics for inputs with different rising edges. Here we set the system to be weak-coupling regime ($2\kappa < \frac{1}{\tau_{ch}} - \frac{1}{\tau_m}$). With ultrafast rising edge, the energy conversion from chaotic fields to WGM (Fig. S4a). Slower rising edge results in the majority of mode coupling to chaotic mode, as shown in the rising chaotic mode intensity in Fig. S4b). Similar dynamics are

shown within the strong coupling regime ($2\kappa > \frac{1}{\tau_{ch}} - \frac{1}{\tau_m}$). In strong coupling regime, the fields oscillate between the WGM and Chaotic fields, with energy exchange rate increase with κ. The oscillation between WGM and chaotic modes within the strong chaotic mode-WGM coupling region, which is likely to be the origin and nondeterministic final states.

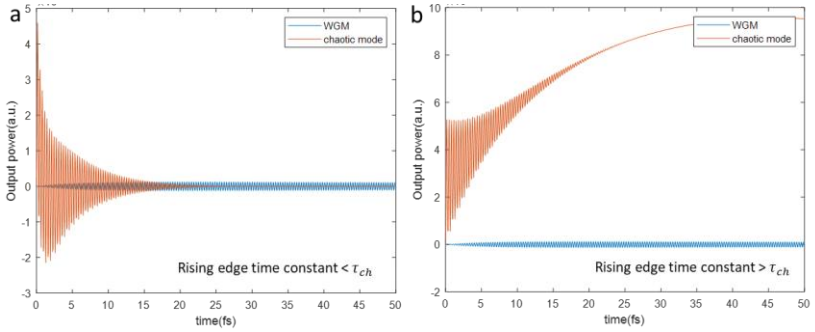

Fig. S5 | Cavity field dynamics in chaotic mode (orange) and WGM (blue) under excitation with different rising edge constants. (a) Rising edge faster (b) slower than the photon lifetime of chaotic mode.

Once the system is stabilized after the fast-rising edge, the WGM proportion ($\eta(t)$) can be expressed as.

$$\eta(t) = \frac{n_m}{n_o + n_m} = \frac{2\kappa}{\gamma_m - \gamma_o + 2\kappa + \sqrt{(\gamma_o - \gamma_m)^2 + 4\kappa} coth coth\left(\frac{1}{2}t\sqrt{(\gamma_o - \gamma_m)^2 + 4\kappa}\right)} \quad \text{(S3)}$$

Where $\eta(t)$ is the WGM proportion with respect to time. Using equation (S-3), we fit our simulation data and extracted the parameters: $\gamma_m = 0.009$, $\gamma_c = 0.02$, and $\kappa = 0.0005$. The extracted parameters align well with our simulation results. The chaotic field decay rate is faster than the WGM decay rate, which is expected since chaotic fields dissipate more quickly over time, leaving only the WGM port after their dissipation. Furthermore, the small value of suggests minimally effective tunneling between the two states.

$\eta(t)$ can also be obtained from the full field numerical simulations. By placing a waveguide cross-sectional monitor in the ring, we retrieved the instantaneous WGM portion by using Equation 1 [S8]. The WGM portion is calculated by projecting the instantaneous electric field onto the established WGM electric field. This allows us to quantify the portion of the mode converted to the WGM during the process:

$$\eta_{WGM}(t) = \left| \frac{\int E(t;x,y,z) E^*_{WGM}(x,y,z) dxdydz}{\sqrt{\int |E(t;x,y,z)|^2 dxdydz \int |E_{WGM}(x,y,z)|^2 dxdydz}} \right| \quad \text{(S4)}$$

Where $\eta(t)$ is the WGM proportion of the mode, which evolves rapidly with time. E is the transient complex electric field in the specific location (x,y,z), while E_{WGM} is the corresponding field of WGM mode at the same location.

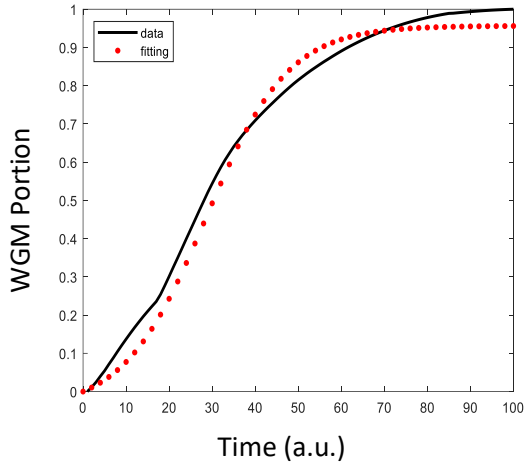

In Fig. S6, we compare the numerically extracted $\eta(t)$ (from equation S4) and the fitting with analytical model (equation S3).

Figure S6 | Coupled mode theory fitting for the chaotic mode – WDM conversion. Dark solid curve: numerical simulation. Dots: two-state CMT models in equation S1.

S3. Time-bin characterization of stochastic switching dynamics

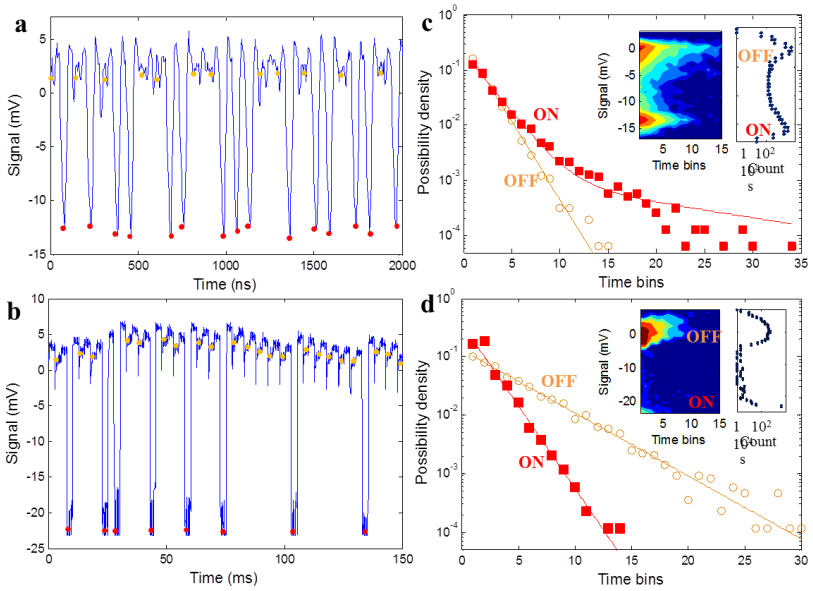

Figure S7 | Stochastic switching dynamics with periodic perturbation, for the ring with 70um radius. The temporal response of the bistable system to the modulated laser signal with peak power at 0.4mW and chopping frequency at (a) 13MHz (b) 200Hz. The red and yellow dots mark points sampled for the 'off' and 'on' states. The laser is set on resonance with the ring resonance at

1484.57nm. (c) and (d) are the ON and OFF time possibility distribution for (a) and (b) respectively. The total data points are 16,000 for both of the plots. The insets are the output signal collected on photodetector versus time bins (left) and histograms for both states. The distribution follows exponential decay: $P=P_0e^{-t/t0}$ (c) f=13MHz: P_{0_ON}=0.130, T_{0_ON}=2.01, P_{0_OFF}=0.165, T_{0_OFF}= 1.53; (d) f=200Hz: P_{0_ON}=0.196, T_{0_ON}=1.53, P_{0_OFF}=0.103, T_{0_OFF}= 4.03.

The switch-on possibility jumps from 0.2 to 0.8 when the detuning is less than 1. The laser repetition period is adjusted between 76 ns to 5 ms. Stochastic switching is observed under both conditions as shown in Fig. S5a-b, but the statistics, including possibility density versus time bins for both ON and OFF states, are significantly different (Fig. S5c-d).

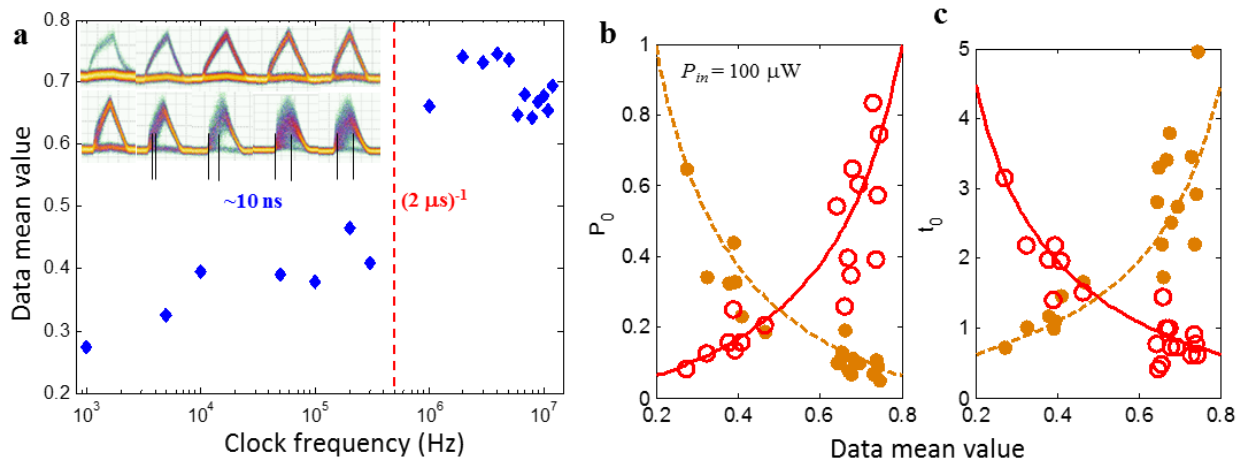

Figure S8 | Laser modulation frequency dependent data statistics. a, Switch-on possibilities (data mean value) versus clock frequency for the device with rectangular waveform drive, with clock frequencies from 1 to 50 MHz, for P_{in} of 100 μW. Inset: eye diagram for triangular waveform drive. **b** and **c,** Amplitude P_0 and lifetime t_0 versus switch-possibility for the on- (red) and off- (orange) states. The red crosses are experimental data for on-states, and the orange dots are for off-states. Statistical models for on- and off-states are illustrated in the red solid and the orange dashed curves respectively.

S4. Detuning and polarization dependence of the statistical binary outputs

For examining the resonance behavior of the random switching, we measure both frequency domain dependence of extinction ratio and time domain SSR. We see the clear detuning and

polarization-dependent SSR resembling the ring transmission measured at CW laser input. It excludes the involvement of optical nonlinearity from the light-ring interaction in the mechanism of random switching (Fig. S7). The polarization and detuning-dependent PSD are plotted accordingly.

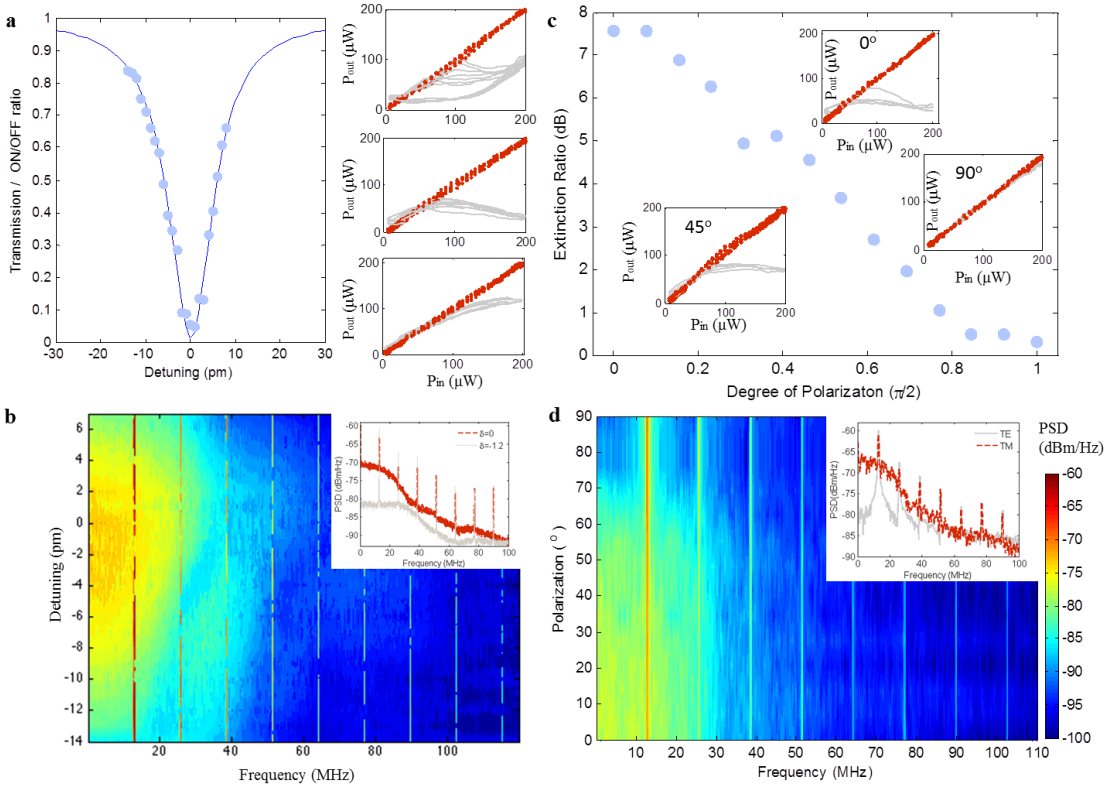

Figure S9 | Detuning and polarization-dependent signal levels of on and off states (a) Transmission spectrum (Solid blue line) of a single resonance located at 1493.104nm with 10.66pm FWHM (middle). The hysteresis loop for the different laser-cavity detunings at -4, 0, and 4 pm (subplot 1-3). The light blue dots are experimental measurements, and the blue curve is the coupled mode theory curve fitting). (b) Correspondent power density for different detunings as shown in a. Inset: the PSD for 0 detuning (red) and -1.2 detuning (grey) (c) Extinction ratio between ON and OFF states as the on-resonance laser polarization tuned from TE to TM in step of 7°. Insets: the hysteresis loop for TE (0°), TM (90°), and in between (45°). (d) Correspondent power density spectrum for TE to TM polarized light, as shown in (c). Inset: PSD for TE and TM polarized light.

Supplementary References:

[SR1] S. C. Mao, S. H. Tao, Y. L. Xu, X. W. Sun, M. B. Yu, G. Q. Lo, and D. L. Kwong, Low propagation loss SiN optical waveguide prepared by optimal low-hydrogen module, Opt. Express 16(25), 20809–20816 (2008)

[SR2] K.-H. Kim, E. V. Johnson, A. G. Kazanskii, M. V. Khenkin, and P. Roca i Cabarrocas. Unravelling a simple method for the low temperature synthesis of silicon nanocrystals and monolithic nanocrystalline thin films. *Scientific Reports* 7, 40553 (2017).

[SR3] D. V. Tsu, G. Lucovsky, and B. N. Davidson, Effects of the nearest neighbors and the alloy matrix on SiH stretching vibrations in the amorphous SiO_r: H (0< r< 2) alloy system, *Physical Review B* **40**, 1795 (1989).

[SR4] J. Fandina, A. Ortiz L. Rodriguez-Fernandez, and J. C. Alonso, Composition, structural, and electrical properties of fluorinated silicon–nitride thin films grown by remote plasma-enhanced chemical-vapor deposition from SiF_4/NH_3 mixtures, *J. Vac. Sci. Tech. A* **22**, 570 (2004).

[SR5] Y. N. Volgin and Y. I. Ukhanov, Vibration spectra of silicon nitride, *Optics and Spectroscopy* **38**, 412 (1975).

[SR6] N. Wada, S. A. Solin, J. Wong, and S. Prochazka, Raman and IR absorption spectroscopic studies on α, β, and amorphous Si_3N_4, *Journal of Non-Crystalline Solids* **43**, 7 (1981).

[SR7] K. O. Bugaev, A. A. Zelenina and V. A. Volodin, Vibrational spectroscopy of chemical species in silicon and silicon-rich nitride thin films, *International Journal of Spectroscopy* **2012**, 291951 (2012).

[SR8] X. Jiang, L. Shao, S.-X. Zhang, X. Yi, J. Wiersig, L. Wang, Q. Gong, M. Lončar, L. Yang, and Y.-F. Xiao. Chaos-assisted broadband momentum transformation in optical microresonators. *Science* 358, 344-347 (2017).

[SR9] H. Lee, L. Chang, A. Kecebas, D. Mao, Y. Xiao, T. Li, A. Alù, S. K. Özdemir, and T. Gu. Chiral exceptional point enhanced active tuning and nonreciprocity in micro-resonators. *Light: Science & Applications* 14, 45 (2025).